Published in final edited form as:
J Magn Reson. 2007 March ; 185(1): 152–158.

Spatially Uniform Sampling in 4-D EPR spectral-spatial imaging

Kang-Hyun Ahn[1,2] and **Howard J. Halpern**[*,1,2]

1 *Department of Radiation and Cellular Oncology, University of Chicago, Chicago, Illinois*

2 *Center for EPR Imaging in Vivo Physiology, University of Chicago, Chicago, Illinois*

Abstract

4-D EPR imaging involves a computationally intensive inversion of the sampled Radon transform. Conventionally, N-dimensional reconstructions have been carried out with N-1 stages of 2-D backprojection to exploit a dimension-dependent reduction in execution time. The huge data size of 4-D EPR imaging demands the use of a 3-stage reconstruction each consisting of 2-D backprojections. This gives three orders of magnitude reduction in computation relative to a single stage 4-D filtered backprojection. The multi-stage reconstruction, however, requires a uniform angular sampling that yields an inefficient distribution of gradient directions. We introduce a solution that involves acquisition of projections uniformly distributed in solid angle and reconstructs in three 2-D stages with the spatial uniform solid angle data set converted to uniform linear angular projections using 2-D interpolation. Images were taken from the two sampling schemes to compare the spatial resolution and the line width resolution. The degradation in the image quality due to the additional interpolation was small, and we achieved ~30% reduction in data acquisition time.

Keywords

EPR; 4-D EPRI; Tomography; Spectral-spatial imaging; Uniform sampling

Introduction

Electron paramagnetic resonance imaging (EPRI) has been successfully applied to biological systems to quantify physiologic parameters, most importantly tissue oxygenation based on spectral linewidth imaging [1-6]. One can extract information about the local fluid environment from the EPR spectrum, which is obtained for each spatial voxel in a 4-D spectral-spatial image [2,7]. The extremely short relaxation time of the electron spin system makes the continuous wave (CW) EPRI technique accessible for most applications. Filtered back-projection (FBP) is commonly used for image reconstruction in CW EPRI [8-12].

Conventionally, FBP for N-dimensional image reconstruction has been carried out with N-1 stages of 2-D backprojection to exploit a dimension-dependent reduction in execution time. Although the multi-stage reconstruction is mathematically equivalent to the single stage reconstruction, it imposes a sampling constraint that projections are aligned in a grid defined, for a 3-D image, by azimuthal and polar angles. In this framework, sampling at uniform linear angles ends up with a non-uniform distribution of gradient directions, with the directions about

*Correspondence: Howard J. Halpern Department of Radiation and Cellular Oncology, MC1105 University of Chicago Medical Center 5841 S. Maryland Ave. Chicago, IL 60637 E-mail address: h-halpern@uchicago.edu Telephone: +1-773-702-6871 Fax: +1-773-702-5940

the poles more densely sampled than at the equator. The inefficiency in the data acquisition is a price that one has to pay for the fast computing with the use of a multi-stage reconstruction.

Recent improvement of PC performance realizes a single stage reconstruction in a reasonable computing time for 3-D EPR images taken with uniform solid angle sampling [13]. However, the huge data size of 4-D EPR imaging inflicts a heavy load of computation, and demands the use of a 3-stage reconstruction that can achieve three orders of magnitude reduction in computation. We devised an imaging procedure that acquires projections uniformly distributed in spatial solid angle and reconstructs in three 2-D stages. The uniform solid angle data set is converted to uniform linear angular projections using 2-D interpolation. With uniformly distributed directions of gradient, we reduce spatial sampling without significant loss of the bandwidth. Our method, however, involves an additional interpolation step that may degrade image quality. We tested the new procedure and compared it with the conventional EPRI. The important figures of merit that characterize the quality of 4-D EPRI are spatial resolution and line width resolution. With an acceptable degradation in these image qualities, we achieved ~30% reduction of data acquisition time that comes from avoidance of inefficiently distributed projections.

Sampling at uniform linear angles brings about spatially crowded projections around the pole. The use of hyperspherical polar coordinates for 4-D EPRI implies the existence of a pole that incorporates a spectral angle as well as spatial angles [14,15] and *vide infra*. We emphasize in the title of this work that the uniformity of the solid angle is not fully four dimensional. There is a similar redundancy in the projections obtained at small gradients or small gradient angles. A fully uniform 4-D solid angle sampling with single stage image reconstruction algorithm will achieve the best tradeoff between image quality and the data acquisition time. This would reduce acquisition of the small gradient angle projections. Unlike the spatial angle sampling, the gradient angle projection sampling involves different signal-to-noise levels at different gradient angles. The low gradient projections have much higher signal-to-noise than those with larger gradients. The reduction of the number of low gradient projections is not useful because they are obtained in relatively short time intervals. In addition, the computational complexity for single stage 4-D image reconstruction algorithm is 3 orders of magnitude higher than the 3-stage 2-D backprojection reconstruction algorithm.

Methods

Data Acquisition

We made a hexagonal phantom consisting of 7 capillary tubes with 1.4 mm inner diameter, lengths in the range of 46-53 mm (extending well beyond the resonator) and a distance between samples of 1.6 mm. A small bottle phantom with 9.5 mm inner diameter and 45 mm length was used for images of a homogeneous phantom. The sensitive region of the resonator was 1.6 cm diameter and approximately 2.5 cm along the axis of the resonator. The phantoms were filled with 1 mM deoxygenated OX063 radical (methyl-tris[8-carboxy-2,2,6,6-tetrakis[(2-hydroxyethyl]benzo[1,2-d:4,5-d']bis [1,3]dithiol-4-yl]-, trisodium salt, MW 1427), a kind gift from Nycomed Innovations, Malmo SW. Images of the small bottle phantom were used for a quantitative comparison of the image quality defined in the following section.

We used a spectroscopic imager operating at 250 MHz [16] to take 4-D spectral-spatial EPR images of the phantoms. A single loop-single gap resonator (with a sample holding loop 16 mm in diameter and 15 mm in length) was used with a circulator based bridge with quadrature RF detection. Field modulation was produced by a 7.5 cm radius Helmholtz coil pair operating at 4.98 kHz with over-modulation (17 μT modulation amplitude). An accurate line shape simulation allowed operation with high modulation amplitude to increase signal-to-noise ratio (SNR) in images without sacrifice in the determination of the intrinsic line width [17,18]. The

RF power delivered to the resonator was 0.020 mW, which was 10 times lower than the saturation level. 14 spectral projections were employed for each of the spatial angular projections. The spectral projections are characterized in terms of a spectral angle α defined as

$$\tan\alpha = G\Delta L / \Delta B, \quad [1]$$

where G is the gradient magnitude, ΔL is the spatial FOV, ΔB is the spectral FOV [14,15]. The spatial and spectral field of view (FOV) was 30 mm and 0.1 mT, which required maximum gradient of 30 mT/m. To compensate for the low SNR at higher gradient projections, the signal was averaged using, for example, 8 sweeps per projection for the highest gradient. Each sweep was acquired with 256 field points, 3 ms/point, 3 ms time constant, and 12-dB/octave filter using an SR830 lock-in amplifier (Stanford Research Systems, Sunnyvale, CA). The projections were subjected to a Gaussian filter whose width was 3.2 points and then subsampled to 256/3.2=80 points.

Image Reconstruction

Computation used standard PCs running MATLAB (Mathworks, Cambridge, MA) version 7. A C code algorithm called from the MATLAB environment performed the backprojection portion of the reconstruction. 4-D spectral-spatial images of the phantoms were taken with two different sampling schemes. First, the image was taken with conventional sampling using uniform linear angles (Figure 1a). This required 10 evenly spaced azimuthal samples for each of 10 evenly spaced polar angles, which resulted in a non-uniform distribution of gradient directions. The numbers of angular sampling N_{POLAR}, $N_{\mathrm{AZIMUTHAL}}$ over the interval of $[-\pi/2, \pi/2]$ define the polar angular interval $\Delta\theta = \pi/N_{\mathrm{POLAR}}$, and the azimuthal angular interval $\Delta\varphi = \pi/N_{\mathrm{AZIMUTHAL}}$. For a sphere of radius r, the angular intervals subtend arcs of length of $\Delta l_\theta = r\Delta\theta$, and $\Delta l_\varphi = r\sin\theta\Delta\varphi$. The sinogram of the conventional sampling was fed into a 3-stage reconstruction algorithm. The second image (Figure 1b) was taken with 66 projections at uniform solid angular intervals. The centers of the solid angle intervals were determined in the following way. We assigned uniform solid angle to each interval using a constraint of $\Delta l_\theta = \Delta l_\varphi$. The centers of the angular bins were then defined by the following:

$$\begin{aligned} N_{\mathrm{AZIMUTHAL}} &= \mathrm{round}\left(N_{\mathrm{POLAR}}\sin\theta\right), \\ \phi_k &= -\frac{\pi}{2} + \frac{\pi}{N_{\mathrm{AZIMUTHAL}}}\left(k-\frac{1}{2}\right), \quad k = 1, \ldots, N_{\mathrm{AZIMUTHAL}}, \\ \theta_k &= -\frac{\pi}{2} + \frac{\pi}{N_{\mathrm{POLAR}}}\left(k-\frac{1}{2}\right), \quad k = 1, \ldots, N_{\mathrm{POLAR}} \quad . \end{aligned} \quad [2]$$

With $N_{\mathrm{POLAR}} = 10$, Eq. [2] produces 66 locations uniformly populating the unit hemisphere.

A sinogram of uniform linear angles (10 evenly spaced polar and azimuthal angles) was produced from the 66 projections sampled at uniform solid angles using 2D cubic spline interpolation at each polar angle and gradient magnitude. Figure 2 demonstrates the procedure of azimuthal angular interpolation for a specific polar angle nearer the polar axis (θ=27°) and a polar angle nearer the equator (θ=63°). The interpolated sinogram was used for the 3-stage reconstruction of the image taken with uniform solid angular sampling.

Characterization of Image Quality

The image qualities were compared using two figures of merit: spatial resolution and line width resolution. Methods to evaluate spatial resolution are well established in imaging theory [19, 20]. The deterministic blurring properties of linear shift-invariant imaging systems can be characterized by a response or spread function. We used an edge spread function, which is the response of the system to an edge source modeled by a 2-dimensional step or Heaviside function [21]. It is mathematically equivalent to the indefinite integral of a line spread function [20].

Figure 3 demonstrates the use of the edge spread function. The rise of signal intensity profile from a simulated phantom image is fitted to an error function, from which full width at half maximum (FWHM) of the line spread function can be extracted. For this work two points separated by one FWHM are taken to be resolved. This definition of resolution is a good surrogate for the classical Rayleigh criterion where two points of equal intensity are said to be resolved if the intensity between them drops to 81% of the maximum [22].

Currently, with conventional PCs, we can reconstruct a 4-D image with maximum number of bins 152 for each dimension, which occupies 2 GB (= $152^4 \times 4$ bytes) of memory when each spectral value is represented as a single precision number. For a practical convenience regarding processing time and memory, we use projections subsampled to a smaller number of bins than the maximum possible. With 80 bins for each dimension, the spatial FOV of 30 mm defines the voxel linear dimension of $30\sqrt{2}/80 = 0.53$ mm, which has a non negligible effect on spatial resolution measurement.

To analyze the effect of finite voxel size, we reconstructed the image using various numbers of bins from 30 to 150. The voxelation was approximated as a Gaussian spread function, whose width is linearly proportional to the voxel size. Then, the measured spatial resolution S can be specified as a convolution of the intrinsic spatial resolution S_I and the Gaussian spread function. This leads to the following quadrature addition.

$$S^2 = S_I^2 + (kD)^2 \quad [3]$$

where k is a dimensionless constant that characterizes the effect of voxel size D. The measurements of spatial resolution from images reconstructed with various numbers of bins were fitted to Eq. [3] to estimate the intrinsic spatial resolution.

A second figure of merit for these images is line width resolution. This translates into oxygen resolution through the linear relationship between oxygen concentration and line width [2]. Figure 4a shows the small bottle phantom, and its EPR spatial image is shown in Figure 4b. From each spatial voxel an EPR spectrum is derived. After selection of voxels with intensity amplitude at least 15% of that of the maximum, the fitting algorithm [17,18] was used to extract the Lorentzian line width from each voxel spectrum. In Figure 5, we display a single plane slice of small bottle phantom showing the fitted line width (Figure 5a) that corresponds to the shaded vertical section of Figure 4b. A histogram of line widths from all of the voxels of the bottle is shown in Figure 5b. The standard deviation of the line width distribution is a quantity that increases as SNR goes down, and was chosen to characterize the line width resolution of the image. Frequently, the line width distribution was accompanied by outliers that unduly degraded the line width estimation. These outliers were mostly from edge artifact and were successfully removed with erosion of the edge voxels (Figure 5c, 5d). The line width resolution was defined as a standard deviation of the line width distribution obtained from the voxels of the bottle with 2 outer layers eroded.

Results

Quantitative Comparison of Image Quality

The data acquisition time was 68 minutes for the 100 uniform linear angular projections and was 45 minutes for the 66 uniform solid angular projections. The latter required an additional interpolation step (Figure 2) achieved in less than a second using a PC equivalent to a 2 GHz Intel Pentium 4. The three stage 4-D image reconstruction took 130 seconds.

The spatial resolution was measured at 10 places along the Z direction on one side of the bottle, and at 10 places along the same direction on the other side of the bottle (Figure 6). This amounts

to 20 measurements of spatial resolution along the direction parallel to the pole, around which projections are densely populated with uniform linear angles. We also obtained 20 measurements of spatial resolution along the direction perpendicular to the pole. The comparison of the two sampling schemes at the two different directions is shown in Table 1. Sampling at uniform solid angles achieved ~30% reduction in data acquisition time with a 12% degradation in spatial resolution. Note the residual asymmetry of the resolution parallel and perpendicular to the polar axis even with the uniform solid angle sampling.

The above procedure was repeated for the images reconstructed with numbers of bins varying from 30 to 150 to analyze the effect of voxel size. Figure 7 shows the measurements of spatial resolution converge toward the intrinsic spatial resolution as the voxel size decreases. The estimated intrinsic FWHM values for the two sampling schemes at the two perpendicular directions are shown in Table 2.

Extraction of line width from the 4-D image produced a 3-D line width map of 80×80×80 matrix, where each dimension corresponded to $3\sqrt{2}$ cm. There were approximately 9300 voxels in the phantom before erosion. The number of voxels in the phantom after two outer layers eroded was ~4100. Line width means and resolutions are displayed in Table 3, which indicates no significant difference.

The EPRI procedure of the small bottle phantom was simulated with the incorporation of experimental noise power spectrum. The simulation was carried out with various numbers of spatial samples. Figure 8a shows the uniform solid angle approach outperformed the uniform linear angle approach in terms of the linewidth resolution. Both sampling methods reached the same spatial resolution with the number of projections over 66 (Figure 8b).

Imaging of Hexagonal Phantom

We took EPR images of the hexagonal phantom (Figure 8a) composed of 1.4 mm id by 0.1 mm wall capillary tubes embedded in a nonparamagnetic elastomer cast with sampling at 100 uniform linear angles (Figure 8b) and with sampling at 66 uniform solid angles (Figure 8c). It demonstrates a remarkable difference in the image quality between the non-uniform distribution and the uniform distribution of projections. The difference was dependent on the geometry of the phantom, and we validated this observation with computer simulation. Synthetic hexagonal phantoms were designed with two different orientations (Figure 9). These phantoms were associated with the simulated spectrum of OX063, and were sampled with the above schemes using the same effective spectral and spatial FOV. The image reconstructed with projections sampled at uniform linear angles, which has projections densely sampled along Z direction, revealed a difference in its performance depending on the phantom rotation. Sampling at uniform solid angles, however, was relatively insensitive to the phantom rotation.

Discussion

We took images of a small bottle phantom using the two sampling schemes, and examined the image quality in terms of spatial resolution and line width resolution. Sampling at uniform linear angles, producing a densely sampled area around the pole, manifested the resolution asymmetry originating from the nonuniform distribution of projections. The use of an edge spread function was useful to quantify the spatial resolution, and identified the anisotropy of spatial resolution.

Images taken from the hexagonal phantom displayed an interesting geometric effect. The Z direction is the more densely sampled direction for uniform linear angle sampling. The configuration of the top phantom in Figure 9a has a projection in the X direction with 5 distinct intensity peaks, and has a projection in the Z direction with 3 distinct intensity peaks. In other

words, it requires more resolving power along the X direction. With the same argument, we can characterize the Z direction of the bottom phantom as requiring more resolving power. We note that the closely packed projections in the Z direction poorly reconstruct the configuration of the top phantom when sampling at uniform linear angles. This was verified in Figure 9b, which is the simulation result of sampling at uniform linear angles for each rotational configuration.

Recently, an adaptive data acquisition strategy has been developed to adjust the distribution of projections such that significant projections are acquired preferentially [13]. The results of Figure 9b support the idea of adaptive acquisition for the phantom with a certain symmetry. The above argument about the phantom configuration can be reiterated in terms of projection information, and Figure 9b shows a detrimental effect when the number of projections is increased in the direction that retains a relatively small amount of information.

For animal experiments, such as oxygen imaging in a murine tumor, it is unlikely that the line width distribution has such a conspicuous directional dependence. Sampling that ensures a good image quality irrespective of phantom geometry will be good enough to serve for practical animal imaging. The simulation result of sampling at uniform solid angles is shown in Figures 9c. It implies that the sampling scheme is relatively insensitive to the configuration of the phantom. Interestingly, as shown in Tables 1 and 2, there still is some spatial resolution asymmetry with uniform solid angle sampling. We hypothesize that this is due to the asymmetric interpolation necessary to use the multistep 2-D reconstruction.

To obtain line width resolution, we computed the standard deviation of the eroded line width map. In Table 3, compared with the image sampled at 100 uniform linear angles, no significant difference of line width resolution was observed with the image sampled at 66 uniform solid angles. The reduction in the number of sampling around the over-sampled area and the additional interpolation for multi-stage reconstruction did not degrade the line width resolution.

Conclusions

We devised a 4-D EPR imaging procedure that acquires projections at spatially uniform solid angles and reconstructs the image with interpolated projections at uniformly distributed azimuthal and polar angles. The image obtained from the new procedure was compared with the image sampled at uniform linear angles. A small degradation of spatial resolution was observed, and the line width resolution did not change. In this way, we reduced the data acquisition time by ∼30%, and still allowed the use of a fast multi-stage reconstruction.

Acknowledgments

The authors would like to thank Dr. Charles A. Pelizzari for useful discussions and critical reading of the text. This work was supported by NIH grants P41-EB002034 and CA-98575.

References

1. Dreher MR, Elas M, Ichikawa K, Barth ED, Chilkoti A, Rosen GM, Halpern HJ, Dewhirst M. Nitroxide conjugate of a thermally responsive elastin-like polypeptide for noninvasive thermometry. Med. Phys 2004;31:2755–2762. [PubMed: 15543780]
2. Elas M, Williams BB, Parasca A, Mailer C, Pelizzari CA, Lewis MA, River JN, Karczmar GS, Barth ED, Halpern HJ. Quantitative tumor oxymetric images from 4D electron paramagnetic resonance imaging (EPRI): Methodology and comparison with blood oxygen level-dependent (BOLD) MRI. Magn. Reson. Med 2003;49:682–691. [PubMed: 12652539]
3. Halpern HJ, Chandramouli GV, Barth ED, Yu C, Peric M, Grdina DJ, Teicher BA. Diminished aqueous microviscosity of tumors in murine models measured with in vivo radiofrequency electron paramagnetic resonance. Cancer Res 1999;59:5836–5841. [PubMed: 10582707]

4. Kuppusamy P, Li HQ, Ilangovan G, Cardounel AJ, Zweier JL, Yamada K, Krishna MC, Mitchell JB. Noninvasive imaging of tumor redox status and its modification by tissue glutathione levels. Cancer Res 2002;62:307–312. [PubMed: 11782393]
5. Sotgiu A, Mader K, Placidi G, Colacicchi S, Ursini CL, Alecci M. pH-sensitive imaging by low-frequency EPR: a model study for biological applications. Phys. Med. Biol 1998;43:1921–1930. [PubMed: 9703055]
6. Matsumoto A, Matsumoto S, Sowers AL, Koscielniak JW, Trigg NJ, Kuppusamy P, Mitchell JB, Subramanian S, Krishna MC, Matsumoto K. Absolute oxygen tension (pO2) in murine fatty and muscle tissue as determined by EPR. Magn. Reson. Med 2005;54:1530–1535. [PubMed: 16276490]
7. Kuppusamy P, Chzhan M, Samouilov A, Wang P, Zweier JL. Mapping the spin-density and lineshape distribution of free radicals using 4D spectral-spatial EPR imaging. J. Magn. Reson 1995;107:116–125.Series B
8. Berliner LJ, Fujii H, Wan XM, Lukiewicz SJ. Feasibility Study of Imaging a Living Murine Tumor by Electron-Paramagnetic Resonance. Magn. Reson. Med 1987;4:380–384. [PubMed: 3035320]
9. Eaton SS, Maltempo MM, Stemp EDA, Eaton GR. Three-Dimensional EPR Imaging with One Spectral and Two Spatial Dimensions. Chem. Phys. Lett 1987;142:567–569.
10. Kuppusamy P, Chzhan M, Vij K, Shteynbuk M, Lefer DJ, Giannella E, Zweier JL. Three-dimensional spectral-spatial EPR imaging of free radicals in the heart: a technique for imaging tissue metabolism and oxygenation. Proc. Natl. Acad. Sci. USA 1994;91:3388–3392. [PubMed: 8159757]
11. Nicholson I, Robb FJ, McCallum SJ, Koptioug A, Lurie DJ. Recent developments in combining LODESR imaging with proton NMR imaging. Phys Med Biol 1998;43:1851–1855. [PubMed: 9703047]
12. Sotgiu A, Placidi G, Gualtieri G, Tatone C, Campanella C. EPR Imaging In Biological Applications - Towards Microtomography. Magn. Reson. Chem 1995;33:S160–S165.
13. Deng Y, Kuppusamy P, Zweier JL. Progressive EPR imaging with adaptive projection acquisition. J. Magn. Reson 2005;174:177–187. [PubMed: 15862233]
14. Lauterbur PC, Levin DN, Marr RB. Theory and Simulation of NMR Spectroscopic Imaging and Field Plotting by Projection Reconstruction Involving an Intrinsic Frequency Dimension. J. Magn. Reson 1984;59:536–541.
15. Maltempo MM. Differentiation of spectral and spatial components in EPR imaging using 2-D image reconstruction algorithms. J. Magn. Reson 1986;69:156–161.
16. Halpern HJ, Bowman MK, Spencer DP, Polen JV, Dowey EM, Massoth RM, Nelson AC, Teicher BA. An imaging radiofrequency electron spin resonance spectrometer with high resolution and sensitivity for in vivo measurements. Rev. Sci. Instr 1989;60:1040–1050.
17. Robinson BH, Mailer C, Reese AW. Linewidth analysis of spin labels in liquids. I. Theory and data analysis. J. Magn. Reson 1999;138:199–209. [PubMed: 10341123]
18. Mailer C, Robinson BH, Williams BB, Halpern HJ. Spectral fitting: The extraction of crucial information from a spectrum and a spectral image. Magn. Reson. Med 2003;49:1175–1180. [PubMed: 12768596]
19. Johns, HE.; Cunningham, JR. The Physics of Radiology. 3rd edition. Charles C Thomas; Springfield IL: 1974.
20. Barrett, HH.; Swindell, W. Radiological Imaging. Academic Press; New York: 1981. revised edition
21. Bracewell, RN. The Fourier Transform and Its Applications. 3rd edition. McGraw Hill; Boston: 2000.
22. Lord Rayleigh. Investigations in Optics, with special reference to the Spectroscope. Phil. Mag 1879;8:261–274.

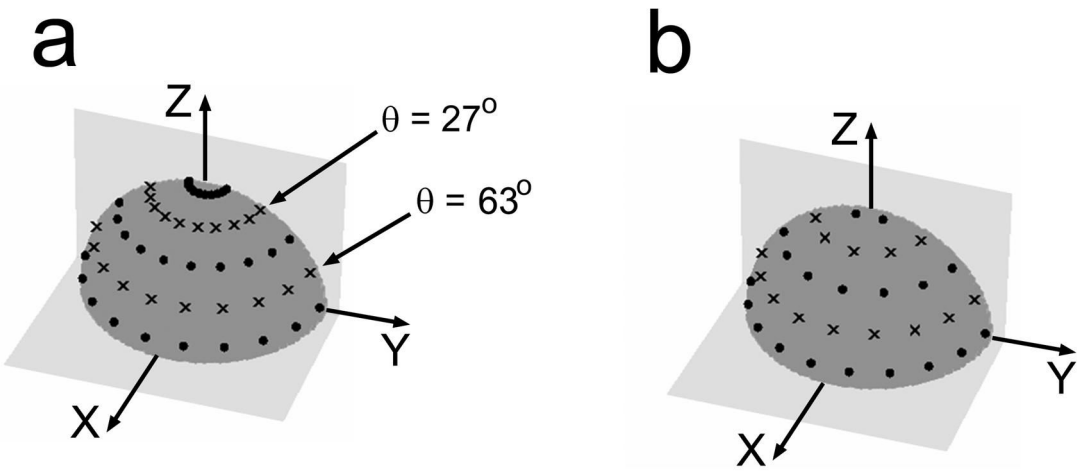

Figure 1.

Two different sampling schemes. Full sampling for both polar and azimuthal angles over [−π/2, π/2] covers the half sphere. The illustration shows sampling of polar angles (θ) over [0, π/2], and sampling of azimuthal angles (φ) over [−π/2, π/2]. (a) Conventional sampling mode requires evenly spaced azimuthal sampling for each of evenly spaced polar angles. This results in a densely sampled area around the pole where polar angle is close to zero. (b) Sampling at uniform solid angles was achieved by modulating the number of azimuthal samples with $\sin\theta$ weighting, where the polar angle θ is uniformly sampled. Each sample occupies the same solid angle to achieve efficient data acquisition. The gradient directions at polar angle 27° and 63° are marked with ×, and the sinograms at these directions are displayed in Figure 2.

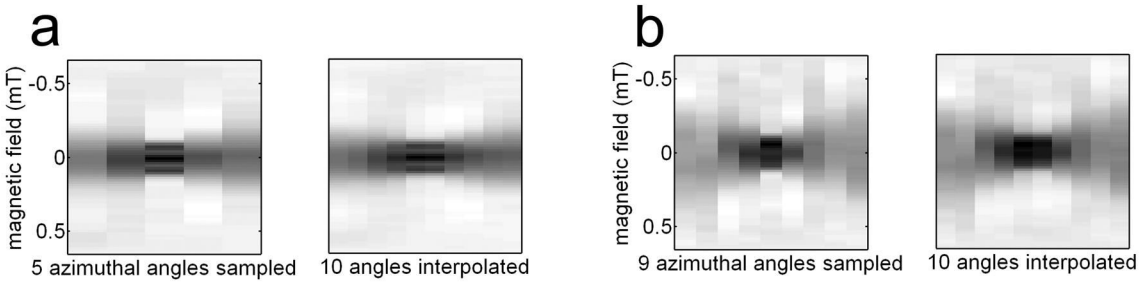

Figure 2.

Demonstration of 2-D interpolation. Sinograms of a hexagonally symmetric phantom: the highest gradient magnitude (a) at polar angle 27° and (b) at polar angle 63° are shown. The spatial positions of these samples are marked with × in Figure 1. The data set sampled at uniform solid angles is converted to that of uniform linear angle to exploit the fast multistage reconstruction algorithm.

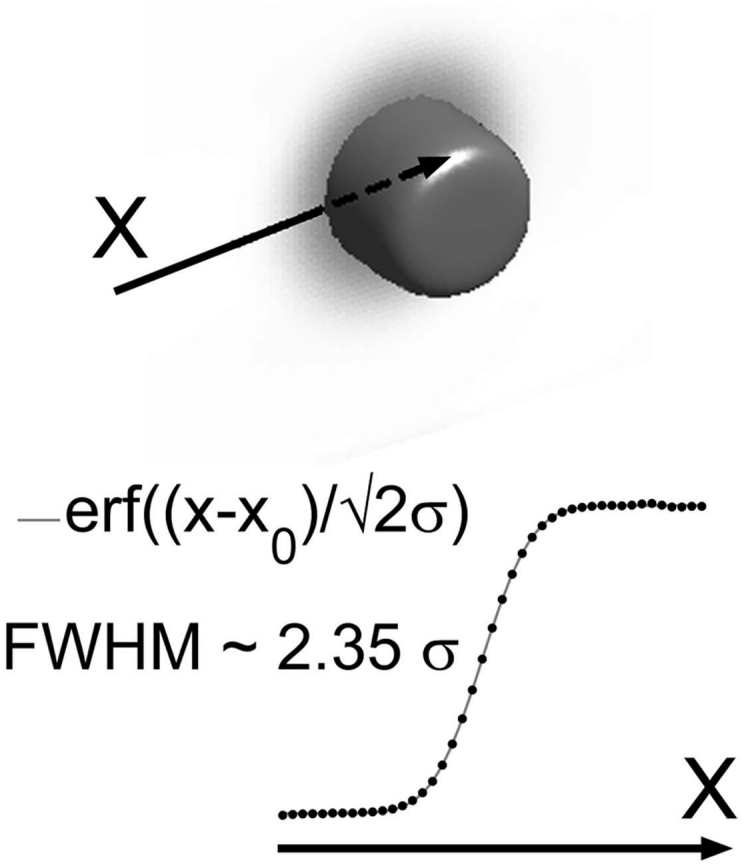

Figure 3.
Measurement of spatial resolution. A cylindrical synthetic phantom was created in which voxels were associated with synthetic EPR spectra of the spin probe. The phantom underwent simulated EPR imaging, and the reconstructed image is shown at the top. An intensity profile along a straight line perpendicular to the surface of the image is plotted at the bottom. The intensity plot, or edge spread function, is fitted to an error function to extract the FWHM of its derivative.

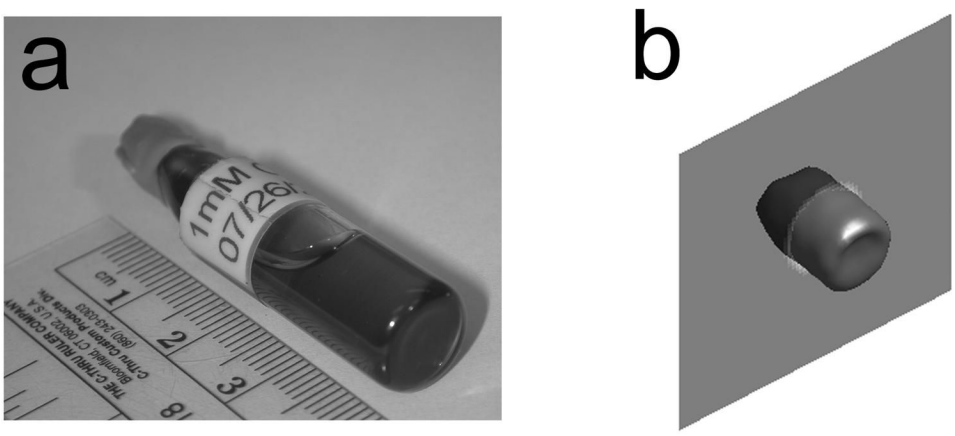

Figure 4.

(a) Photograph of the small bottle phantom used for a quantitative analysis of spatial resolution and line width resolution. (b) EPR spatial image of the small bottle phantom. A concave surface (seen from the outside) is visible which portrays the curved bottom wall of the bottle. The shaded vertical region shows the section of the line width maps in Figure 5. Note that the apparent difference between the EPR image and the photograph is the bottle wall thickness.

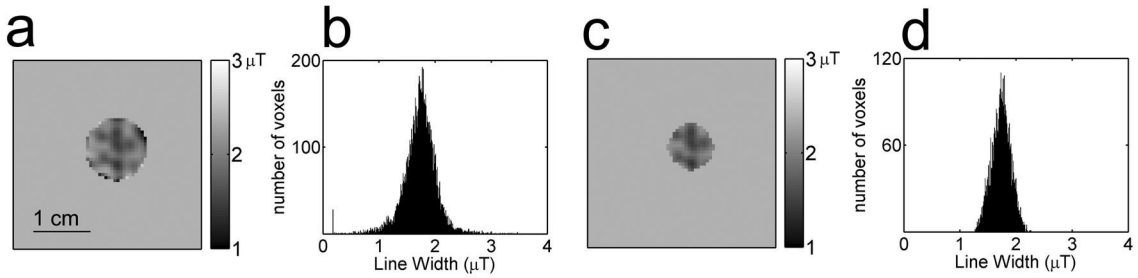

Figure 5.

Measurement of line width resolution. (a) Fitted line width map of the phantom at the section specified in Figure 4b. (b) Histogram of the line width values for voxels in the bottle image. Standard deviation of the distribution can characterize the line width resolution, but the outliers mostly from the edge artifacts unduly degraded the line width estimation. (c) Line width map of the phantom with 2 outer layers eroded at the same section as in (a). The eroded image, smaller than the actual phantom, retained the inherent linewidth variation. (d) Histogram of the line width values for voxels in the eroded image. The outliers were successfully removed by erosion.

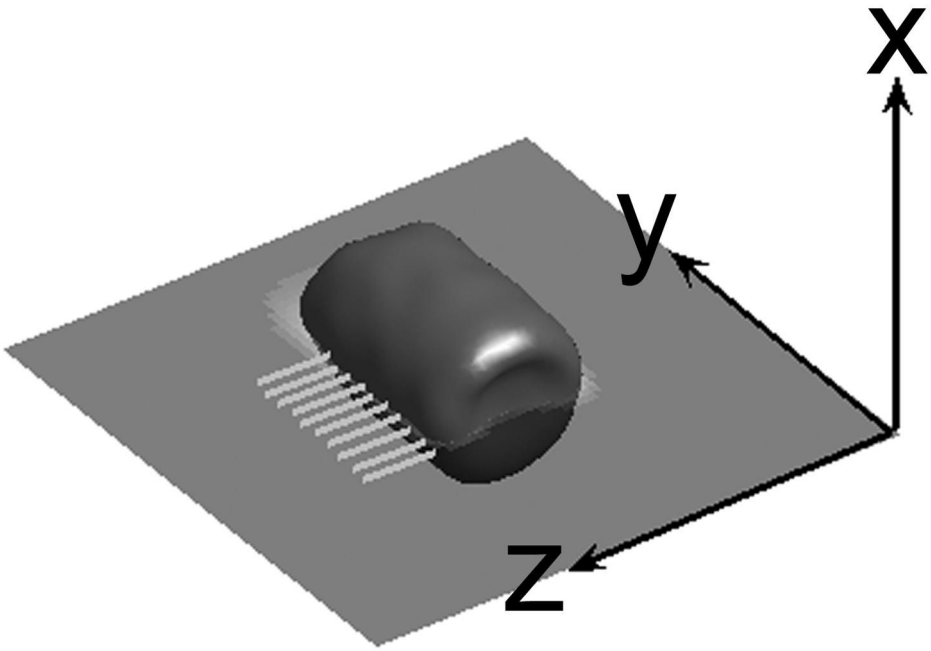

Figure 6.
The spatial resolution was measured along two directions. The comb lines along Z direction in one side of the bottle represent 10 measurements using edge spread function. With another 10 measurements in the other side of the bottle, we obtained 20 samples for spatial resolution along the direction parallel to the pole. The same measurement was carried out along X direction which is perpendicular to the pole.

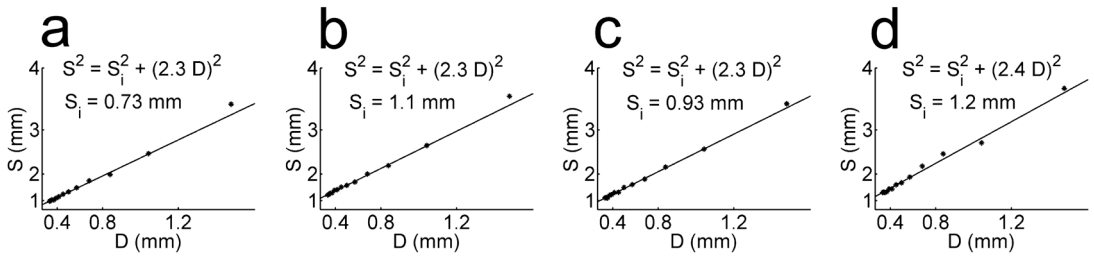

Figure 7.

Spatial resolution S can be specified as a convolution of the intrinsic spatial resolution S_i and the voxelation. As the voxel size decreases, spatial resolution converges toward the intrinsic spatial resolution. Values of FWHM measured from images reconstructed with various numbers of bins are plotted in squared scale to show the relationship of quadrature addition. (a) Uniform linear angles, parallel to the pole. (b) Uniform linear angles, perpendicular to the pole. (c) Uniform solid angles, parallel to the pole. (d) Uniform solid angles, perpendicular to the pole.

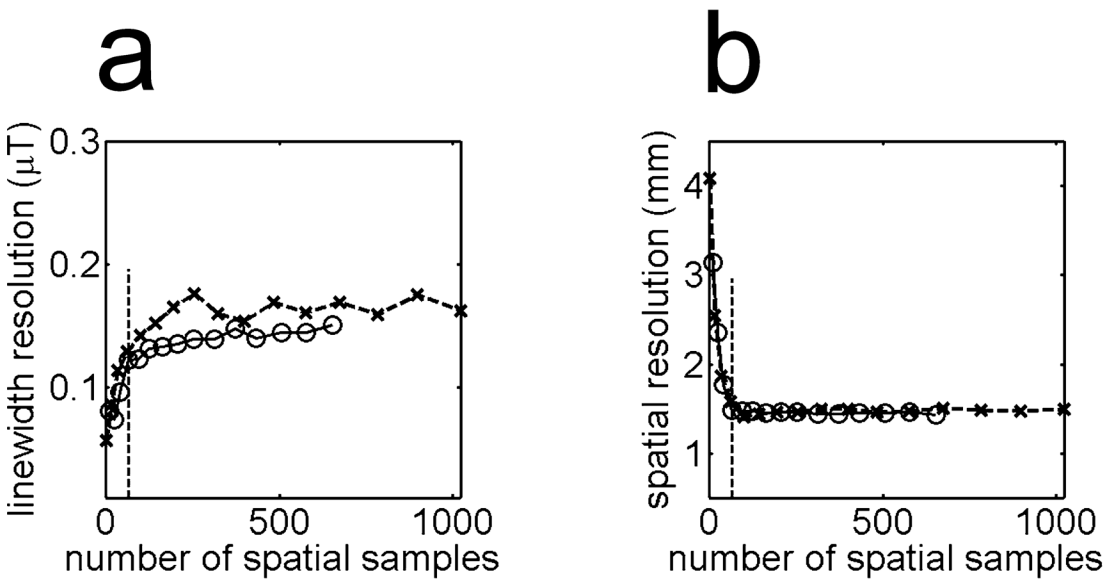

Figure 8.

Simulated results show changes of image qualities with the variation of number of spatial samples. Open circles represent uniform solid angle method, and crosses represent uniform linear angle method. Dotted vertical lines indicate 66 spatial samples. (a) Linewidth resolution. (b) Spatial resolution (average of measurements parallel and perpendicular to the pole).

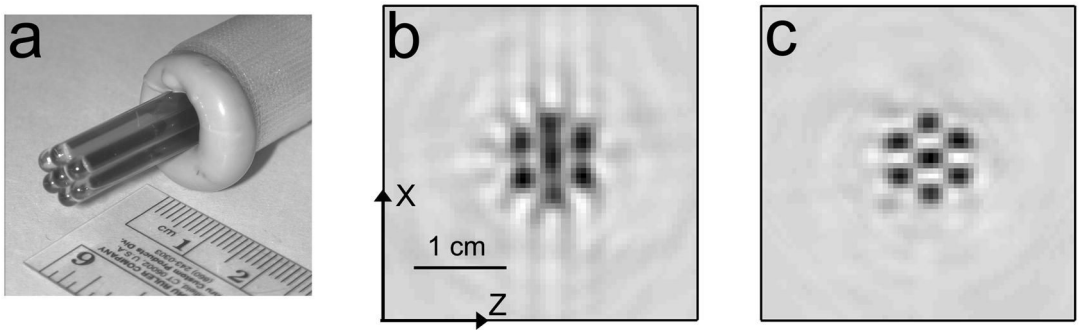

Figure 9.
(a) Photograph of the hexagonal phantom used for a qualitative assessment of spatial resolution. The separation between the liquid samples was approximately around the resolving distance (~1.7 mm). (b) EPR spatial image of the hexagonal phantom taken with sampling at 100 uniform linear angles. The resolving power was better along Z direction, where the sampling was dense. (c) EPR spatial image taken with sampling at 66 uniform solid angles. All 7 tubes were clearly resolved. The poor reconstruction of (b) with larger number of sampling than (c) reveals the risk of the reconstruction with non-uniform spatial resolution, which was further clarified in Figure 9 with simulation.

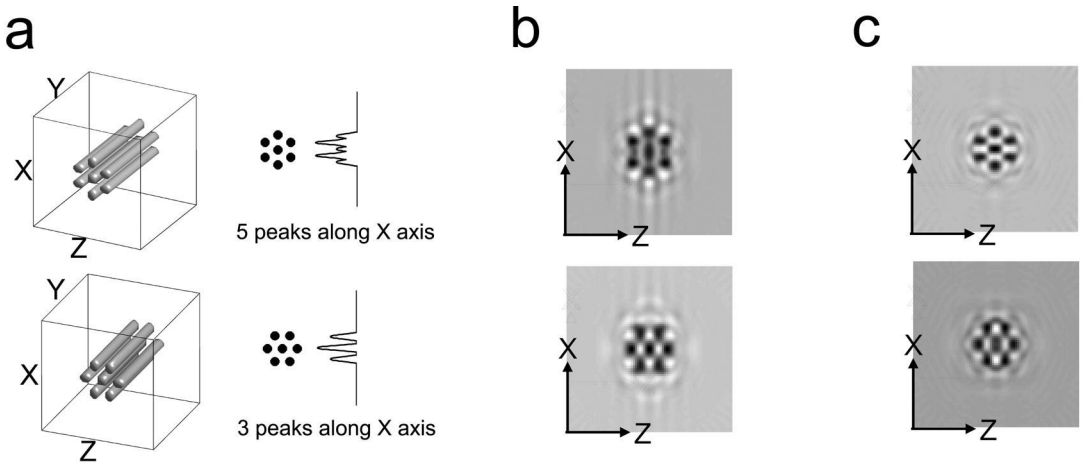

Figure 10.
Simulation results of sampling at uniform linear angles (10 polar × 10 azimuthal) and sampling at 66 uniform solid angles. (a) The configuration of the phantom in the top requires more resolving power along X direction, whereas that in the bottom requires more resolving power along Z direction. (b) Reconstructed images from sampling at uniform linear angles. The gradient directions are denser along Z direction, and the bottom configuration results in a better image compared to the top configuration. (c) Reconstructed images from sampling at uniform solid angles. These are relatively insensitive to the phantom geometry.

Table 1

Comparison of spatial resolution[a] from sampling at uniform linear angles and sampling at uniform solid angles.

	100 unif. linear angles	66 unif. solid angles
parallel to the pole	1.4 ± 0.03 mm	1.6 ± 0.05 mm
perpendicular to the pole	1.7 ± 0.05 mm	1.8 ± 0.08 mm

[a] The spatial resolution was computed from images reconstructed with 80 bins for each dimension.

Table 2

Estimated intrinsic spatial resolution[a] from sampling at uniform linear angles and sampling at uniform solid angles.

	100 unif. linear angles	66 unif. solid angles
parallel to the pole	0.73 mm	0.93 mm
perpendicular to the pole	1.1 mm	1.2 mm

[a] The intrinsic spatial resolution was estimated from images reconstructed with various number of bins.

Table 3

Comparison of line width resolution from sampling at uniform linear angles and sampling at uniform solid angles.

	100 unif. linear angles	**66 unif. solid angles**
line width resolution (SD)	0.17 μT	0.17 μT
mean	1.74 μT	1.75 μT